

Echofilter: A Deep Learning Segmentation Model Improves the Automation, Standardization, and Timeliness for Post-Processing Echosounder Data in Tidal Energy Streams

Scott C. Lowe^{1,2,*}, Louise P. McGarry^{3,*}, Jessica Douglas³,
Jason Newport^{4,5}, Sageev Oore^{1,2}, Christopher Whidden^{1,4}, and
Daniel J. Hasselman³

¹*Faculty of Computer Science, Dalhousie University, Halifax, Nova Scotia, Canada*

²*Vector Institute, Toronto, Ontario, Canada*

³*Fundy Ocean Research Centre for Energy, Halifax, Nova Scotia, Canada*

⁴*DeepSense, Dalhousie University, Halifax, Nova Scotia, Canada*

⁵*Marine Environmental Research Infrastructure for Data Integration and Application Network, Halifax, Nova Scotia, Canada*

Correspondence*:

Scott C. Lowe
scott.lowe@dal.ca

Louise P. McGarry
louise.mcgarry@fundyforce.ca

ABSTRACT

Understanding the abundance and distribution of fish in tidal energy streams is important for assessing the risk presented by the introduction of tidal energy devices into the habitat. However, the impressive tidal currents that make sites favorable for tidal energy development are often highly turbulent and entrain air into the water, complicating the interpretation of echosounder data. The portion of the water column contaminated by returns from entrained air must be excluded from data used for biological analyses.

Application of a single algorithm to identify the depth-of-penetration of entrained-air is insufficient for a boundary that is discontinuous, depth-dynamic, porous, and widely variable across the tidal flow speeds which can range from slack tide to full flow at 5 m s^{-1} .

Here, using a case study at a tidal energy demonstration site in the Bay of Fundy, we describe the development and application of deep machine learning models that produce a pronounced, consistent, substantial, and measurable improvement of the automated detection of the extent to which entrained-air has penetrated the water column.

Our model, Echofilter, was found to be highly responsive to the dynamic range of turbulence conditions and sensitive to the fine-scale nuances in the boundary position, producing an entrained-air boundary line with an average error of 0.32 m on mobile downfacing and 0.5–1.0 m on stationary upfacing data. The model's overall annotations had a high level of agreement with the human segmentation, with a Jaccard index of 98.8% for mobile downfacing recordings and 93–95% for stationary upfacing recordings. This resulted in a 50% reduction in the time required for

manual edits when compared to the time required to manually edit the line placement produced by the currently available algorithms. Because of the improved initial automated placement, the implementation of the models generated a marked increase in the standardization and repeatability of line placement. The machine learning contribution to assessing the ecological impacts of introducing marine renewable energy devices into the habitat is the improved analytical consistency and substantial improvements in the timeliness of analyses and subsequent reporting.

1 INTRODUCTION

The need for clean, non-carbon emitting, generation of electricity is well established. The Intergovernmental Panel on Climate Change (IPCC), the United Nations body for assessing the science related to climate change, summarizes the recent changes in climate as widespread, rapid and intensifying (IPCC, 2021). And that to limit climate change, strong and sustained reductions in emissions of carbon dioxide (CO₂) and other greenhouse gases are required (IPCC, 2021). In an effort to limit climate change and the ensuing effects, attention has turned to renewable, non-carbon emitting electricity-generating technologies such as hydropower, wind, solar, and the marine renewable energies. In the suite of marine renewable energy options, energy extraction from tidal streams is one solution for producing electricity reliably and predictably.

The Bay of Fundy is situated between the Canadian Atlantic provinces of New Brunswick and Nova Scotia. With its extreme tidal range exceeding 16 m in places (Cornett et al., 2015; O'Reilly et al., 2005; Hasegawa et al., 2011) and more than 100 billion tonnes of seawater moving into and out of the Bay twice a day (Cornett et al., 2015; Durand et al., 2008), more than the combined discharge of the world's freshwater rivers (Durand et al., 2008), the Bay has long been a focus of tidal energy discussions in the U.S. and in Canada (Lowrie, 1968). With the advancement of in-stream tidal energy conversion technology, attention has turned to investigating tidal energy development in Minas Passage (Hasegawa et al., 2011; Karsten et al., 2008; AECOM Canada Ltd, 2009; Dupont et al., 2005), the site of the strongest currents in the Bay of Fundy (Karsten et al., 2008) with current speeds up to 5 m s^{-1} (Hasegawa et al., 2011).

In the upper Bay of Fundy, Minas Passage is situated in the southern arm near Parrsboro, Nova Scotia. In 2009, the Fundy Ocean Research Centre for Energy (FORCE)¹ was established and includes a tidal energy demonstration site at Minas Passage. The facilities include five underwater, grid-connected, berths leased to developers for testing and demonstration of in-stream tidal energy conversion devices. Advantages of the multi-berth demonstration site include allowing the developers to share costs, limit potential impact, and test under similar conditions. FORCE contributes to this by undertaking scientific investigations of the environmental and ecosystem conditions at the site. One goal of the work is to understand the potential risk to fish presented by the presence of tidal energy devices in the habitat.

Hydroacoustic methods, applied to data collected with scientifically calibrated echosounders, are used to quantify the distribution and abundance of fish in the marine environment (Benoit-Bird and Lawson, 2016), and commonly used in fisheries science (Fernandes et al., 2002; Johannesson and Mitson, 1983). Echosounders, by emitting a pulse of sound (a "ping") into the water and recording the magnitude of the returned backscatter, are capable of interrogating the entire water column in high resolution in both time and space (Simmonds and MacLennan, 2005). Distinguishing sound scattered from physical interfaces such as the sea floor or sea surface (sea-air interface) and sound scattered from biological sources such as

¹ <https://fundyforce.ca>

fish or zooplankton works very well when the medium (seawater) through which the sound propagates is uniform (Simmonds and MacLennan, 2005), but is challenging when the medium is not uniform.

The impressive, but often highly turbulent, tidal currents (Cornett et al., 2015) favorable to tidal-energy development present special challenges for hydroacoustics in the form of air, an efficient sound-scatterer, entrained into the water column. Given the strongly reflective and non-porous natures of the boundaries at the sea floor and at the sea surface, it is relatively straightforward to identify the position of these surfaces. However, defining the extent of penetration of entrained-air is much more challenging due to the discontinuous, depth-dynamic, porous, and indistinct nature of the boundary of the entrained-air. Given that the goal is to document the distribution and abundance of fish, it is very important that the lines bounding the observable water column (sea floor, sea surface, and the ambit of entrained-air sometimes colloquially referred to as the “turbulence line”) are appropriately defined such that energy returned from physical sources is excluded from biological analyses.

Echoview Software (Echoview Software Pty Ltd. Hobart, Australia) is the international standard for advanced visualization and post-processing of hydroacoustic data. A variety of highly configurable parameterized algorithms with which to estimate the placement of each of the bounding lines are available in Echoview. To increase the efficiency and standardization of line placement, once the algorithms and parameters have been identified, the setup is saved as a template and then applied to the data within each Echoview file. The Echoview-generated lines are then scrutinized by an analyst and parameters modified or line segments adjusted as needed. The lines defining the physical interfaces and a nearfield line (a line set at a constant range to exclude the echosounder “nearfield” in which the sound pulse is not yet organized (Simmonds and MacLennan, 2005)) ultimately define the boundaries of the marine environment suitable for analyses of fish abundance and distribution (see Figure 1).

In relatively benign marine conditions, the Echoview algorithms result in appropriate placement of the lines designating the sea floor and sea surface given their strongly reflective and non-porous natures. However, the algorithms are particularly handicapped at defining the porous, indistinct, and discontinuous end-boundary of the penetration of the entrained-air in turbulent tidal channels. In addition, water flow in tidal energy sites ranges from slack tide to 5 m s^{-1} resulting in a strongly depth-dynamic penetration of the entrained-air further complicating the identification of the end-boundary of entrained-air with a single, parameterized algorithm.

The consequences of applying a single parameterized algorithm to data which encompasses the variable entrained-air conditions encountered throughout the tidal cycle include:

- refinement of the position of the turbulence line requires substantial and time-consuming manual edits,
- the quantity of edits generates analyst fatigue putting at risk the regions where the full force of analyst attention is needed for discerning usable data, and
- standardization and/or repeatability is impossible to achieve between analysts and within the work of a single analyst.

In summary, the state-of-the-art software, Echoview, although highly configurable is based on classical algorithm methods and therefore cannot be sufficiently responsive to the dynamic range of data conditions found at a tidal energy site. To address this shortcoming, we applied machine learning methods to build models which can generate an entrained-air (“turbulence”) line with, as much as possible, the same placement as the examples provided by a human annotator. In so doing, our aim was to develop a model by

which to improve the automated detection of the extent to which entrained-air has penetrated the water column as rendered in hydroacoustic data.

Machine learning allows us to build a model to solve a task by training it on example data. Deep learning in particular allows us to build the large models which are necessary to solve challenging tasks which would otherwise require a human to laboriously perform. In this framework, an artificial neural network is instantiated according to a particular architectural design with randomly initialized parameters, and these parameters are iteratively updated through gradient descent as part of the learning process in order to maximise performance at the objective task. Through this training process, the network learns to approximate a function that maps a set of input stimuli to the correct outputs. A large amount of labelled data comprised of target input/output pairs is required in order to train the network successfully such that it can generalize to unseen stimuli.

In the context of this work, our input to the model is a 2D image-like structure whose axes are depth and time, and the intensity at each pixel is the volume backscattering strength (S_v dB re: 1 m^{-1}). When this data structure is rendered as a plot, it is referred to as an “echogram”. The primary output of our model is a prediction of the depth of the entrained-air boundary line for each point in time (each ping). In addition to this, our model also predicts the depths of the seafloor and sea surface boundary lines.

Our final implementation, *Echofilter*, is openly available under the AGPLv3 license. Python source code and stand-alone Windows executable are available at <https://github.com/DeepSenseCA/echofilter>, with command line interface (CLI) and application programming interface (API) documentation available at <https://DeepSenseCA.github.io/echofilter/>.

The benefits of improved automated detection of the entrained-air line include reducing the time required to post-process hydroacoustic data collected at the tidal energy demonstration site operated by the Bay of Fundy Ocean Research Centre for Energy (FORCE) in Minas Passage, Nova Scotia.

2 MATERIALS AND EQUIPMENT

Hydroacoustic data was collected from two tidal energy demonstration sites in Nova Scotia, Canada: the FORCE-operated site in Minas Passage in which flow speeds can exceed 5 m s^{-1} (Karsten et al., 2011) and a site occupied by Sustainable Marine Energy (Canada) Ltd. in Grand Passage in which flow speeds can achieve 2.5 m s^{-1} (Guerra et al., 2021).

“Stationary” data was collected using a calibrated Simrad EK80 WBAT 7° split-beam echosounder operating in continuous wave (CW) mode at 120 kHz in Minas Passage and in Grand Passage. The echosounder, with its transducer in an upward facing orientation was attached to a platform deployed to the sea floor (see Figure 1). At both data collection sites, maximum seawater depth was less than 50 m. The echosounder was deployed in Minas Passage for three 2-month periods in 2018. Data was recorded every 30 minutes for 5 minutes. Passive data collection with the echosounder in listening-only mode to document system self-noise and record levels of ambient sound present at 120 kHz was collected during two of the three deployments. There were two deployments of the echosounder in Grand Passage during late 2019 and early 2020. In both cases, the echosounder was deployed for less than 14 days. Data collection cycle in Grand Passage consisted of one-hour continuous data collection in alternating hours. Short durations of passive data were collected each hour.

“Mobile” data was collected from the FORCE tidal energy demonstration site using a calibrated Simrad EK80 WBT 7° split-beam echosounder operating in CW mode at 120 kHz. The transducer was deployed in a downward facing orientation attached via polemount to the vessel. The mobile survey pattern consisted of

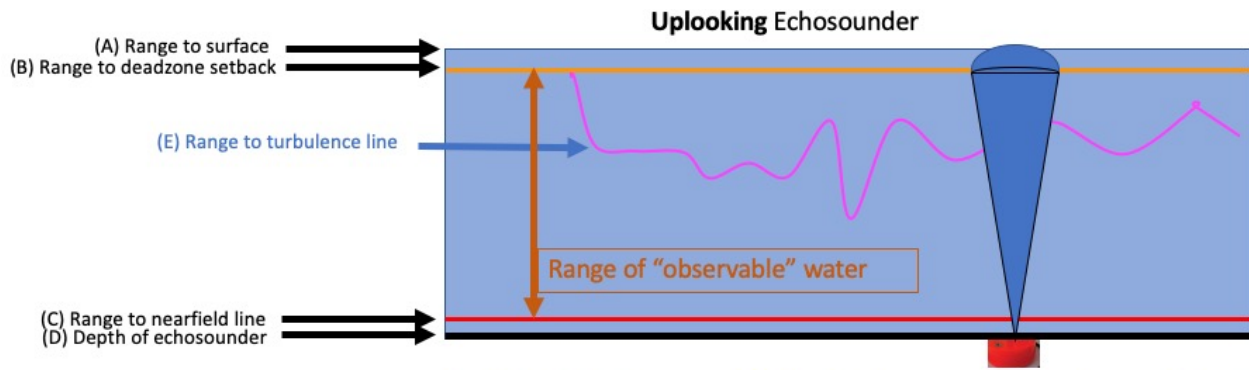


Figure 1 Illustration of the boundaries defining the range of the observable water column for an upfacing echosounder.

a set of six parallel transects 1.8 km in length encompassing the Minas Passage tidal energy demonstration site in the northern portion of the Passage and included three transects located across the Passage near the southern shore. The mobile surveys consisted of discrete 24-hour data collection periods. Seventeen such surveys were conducted between May 2015 and October 2018. Mobile data collection included periods of passive data collection with the transiting of each transect.

The echosounder data files were imported into Echoview (version 10.0) and post-processed in the typical way: assigned calibration parameters, examined the data and removed noise, removed the passive data from further processing, set the line at a constant range from the transducer face (1.8 m in this case) by which to exclude the echosounder nearfield, and apply Echoview algorithms to estimate, for each ping, the position of the sea floor (for downfacing echosounder) or sea surface (for upfacing echosounder) and the depth-of-penetration of the entrained-air. In order to exclude the acoustic deadzone inherent in echosounder data (Simmonds and MacLennan, 2005), a one-meter offset was applied to the bounding line (sea floor or sea surface) and to the entrained-air line.

Table 1 Summary of dataset partitions.

Dataset	Location	Mobility	Orientation	N ^o Recordings			N ^o Pings		
				Train	Val	Test	Train	Val	Test
MP:mob↓	Minas Passage	Mobile	Downfacing (↓)	727	91	245	1.21M	148k	394k
MP:sta↑	Minas Passage	Stationary	Upfacing (↑)	7,249	919	875	2.45M	305k	300k
GP:sta↑	Grand Passage	Stationary	Upfacing (↑)	118	0	28	0.36M	0	96k

The full suite of Echoview files were divided into sets of files for training, validating, and testing the machine-learning models. The mobile downfacing dataset collected at Minas Passage contained a collection of 17 surveys, repeated at the same 10 transects on 17 different days spanning the course of three years. We selected two transects and placed all recordings from these in the test set. The remaining data was partitioned into training and validation partitions with a 89%/11% split, stratified against the season in which the data was collected (winter vs non-winter) to ensure an equal split of the sparser winter recordings. The stationary data was collected continuously, so we simply partitioned the data at random (without stratification). We placed 80% of the MP:sta↑ and GP:sta↑ data in the training partition. For the MP:sta↑ dataset, 10% of the data was used for model validation and 10% for final testing. Due to its smaller size,

we did not use any GP:sta↑ data for the model validation process and kept the remaining 20% of the data for testing. The number of recordings and pings for each partition of each dataset is indicated in Table 1.

Files used for manual evaluation were selected from the MP:sta↑ and GP:sta↑ validation and test partitions. We ensured that, within each of the three stationary deployments in Minas Passage, sufficient files to include 24-hour coverage, not necessarily consecutive, of data collected at neap tide and at spring tide in order to evaluate model performance under best-case and worst-case entrained-air scenarios. To assess the model’s ability to generalise to unseen data in comparison to data on which it was optimised directly during the training process, we also selected files from the MP:sta↑ and GP:sta↑ training partition to manually inspect. These files were selected so as to give 24-hour coverage of data collected at neap tide and spring tide. Specifically, if undesired excursions occurred in the entrained-air line placements within the test files, we needed to determine whether it was a function of running the models on “new” data, indicating an issue with the model’s ability to generalise (overfitting), or whether it was also a problem on the training data, indicating an issue with the model design (underfitting).

3 METHODS

3.1 Data preprocessing

Annotated data was stored in Echoview EV files. These files contain the S_v data, along with human-generated annotations for the lines, and min/max S_v value thresholds. The EV files were opened in Python using win32com to interface with Echoview’s programming interface (API), and exported into several files. The surface, seafloor, and entrained-air lines were exported into Echoview line (EVL) file format. The S_v data was exported into CSV format twice as follows. The first S_v CSV file (“raw S_v CSV”) was exported with all EV exclusion settings disabled, and contained the entire S_v data in the EV file. The second S_v CSV file (“clean S_v CSV”) used the exclusion settings as implemented in the EV file so that all data which should be excluded from ecosystem analyses was masked out, appearing as the NaN indicator value -9.9×10^{37} in the output CSV. This means all datapoints above the entrained-air line, below the seafloor line (for downfacing recordings), passive data, bad data time periods where the analyst deemed a range of pings to contain data too contaminated by returns from entrained air to use at all, and other miscellaneous localised “bad data” caused by anomalous events such as a rope drifting into view which the analyst had labelled for exclusion, were removed from the output (set to the NaN indicator value), leaving only the datapoints deemed as “good data” by the analyst.

Since this export process requires using Echoview to read in and export the data from the EV file, and Echoview is only available for Windows, this first step of the data processing pipeline must be performed on a Windows system with a licensed copy of Echoview installed. The remaining steps in the data processing and model training pipeline only require Python and can be run on any operating system.

The CSV files and EVL files were loaded into Python with a custom data loader. The depth resolution (and number of datapoints) per ping sometimes differed during a recording session, resulting in data with an uneven sampling resolution; we addressed this by finding the modal depth resolution across pings and linearly interpolating the data for each ping onto the same array of depth sample points. We created a “target mask” based on the location of NaN-values in the clean S_v CSV. This target mask corresponds to the overall target for the network’s output. The depth lines loaded from the EVL files were linearly interpolated onto the same set of timestamps as the S_v data.

We observed some discrepancies between the depth lines and the mask, which was caused by 1) off-by-one differences when the line threshold is applied in Echoview compared with our own interpolation of the line; 2) analysts using boxes or freehand regions to annotate exclusion regions which are adjacent to the

boundary lines. We handled this by identifying the upper and lower contiguous extent of the masked out area to generate new lines from the mask. For the entrained-air line, we primarily used the deepest extent of the two options as provided via the line annotation and the mask annotation. For the seafloor line, we primarily used the original line annotation as the network’s output target, but we also produced a second line (with more aggressive removal) which extended higher up the water column to include any additional masked out area. The spare “aggressive” version of the seafloor line was included as an auxiliary target during training.

The surface line annotations were mostly unchanged by the annotators from the output produced by Echoview’s algorithms. These were observed to be mostly accurate, but contained occasional large jumps in value. These outliers were detected and removed by using a median filter as follows. We applied a median filter with a kernel length of 201 and observed the residual between the raw signal and the median filter. Values more than 5 standard deviations (robustly estimated from the interquartile range, $\sigma = \text{iqr}/1.35$) were set to the median value. We then applied a median filter with a kernel length of 31 and removed anomalous values more than 4 standard deviations (robustly estimated from the interdecile range, $\sigma = \text{idr}/2.56$) from the median. The second step was repeated until no anomalies were removed. Additionally, if the surface line was ever deeper than the entrained-air line, we set it to be the same depth as the entrained-air line. We found this anomaly removal process produced surface lines of sufficient quality. For downfacing samples, the surface line was set at 0 m (coincident with the transducer face).

Passive data annotations were taken as hard-coded on/off cycles where known *a priori*. Otherwise, passive data collection periods were identified using a bespoke algorithm. The first S_v responses, corresponding to depths closest to the echosounder, have large intensities when the echosounder is active due to their proximity to the emitter, and much lower values when the echosounder is passive. We identified passive data periods by observing the first 38 depth sample points (after our interpolation step onto a common sampling grid). We took the difference in S_v between consecutive pings, and then the median across the first 38 depth samples for each ping. Median differences which exceeded ± 25 dB were identified as boundary points between passive and active recording periods.

Bad data periods were identified as collections of consecutive pings for which all the data was masked out. Periods of passive data recording were excluded from the bad data periods. Bad data periods in which the entrained-air line was at or below the seafloor line throughout the entire period were also excluded.

Bad data patches were identified by the “pixels” in the echogram which were masked out for any reason not already covered by being above the entrained-air line, below the seafloor line, during a period of passive data collection, or during a period of time identified as a bad data period.

Our data was comprised of both upfacing and downfacing echosoundings. In the recording data structure, and exported CSV files, the y -dimension is stored as increasing distance from the echosounder. To standardize our inputs to the network, we flipped the orientation of the upfacing data such that increasing indices in the y -dimension corresponded to increasing depth within the water column.

The number of timepoints per file was much larger than we could reasonably supply to the network as a single input “image”. Moreover, it is important that a single training batch contains a diversity of training data. To prevent the system from having to read in the contents of an entire recording file when needing to select only a small subset of the data to present for each training step, we broke the training data into chunks (shards) each with a length of 128 samples.

The pipeline for converting the CSV and EVL data into the preprocessed training shards can be executed with the command `echofilter-generate-shards`.

3.2 Training inputs

When analysing echosounder data, it is common practice to offset the seafloor and entrained-air boundary lines by a fixed distance, 1 m for the echosounders used here. The purpose of the fixed-distance offsets are to exclude those portions of the data near boundaries, such as the sea surface or sea floor or the entrained air boundary, that may be biased due to the echosounder deadzone which is a function of the shape of the spherically spreading beam intersecting with a surface (Simmonds and MacLennan, 2005). In addition, it generates a buffer between the boundary of the entrained air and the data reserved for biological analyses, so as to exclude returns from entrained air adjacent to, but not connected to, the pronounced entrained air boundary. This ensures processing errs on the side of excluding slightly more data, instead of accidentally including bad data. Some datasets had an offset of 1 m included in the line definitions, whereas others did not. We standardized this by subtracting offsets from the lines which had them included. Consequently, the model’s target output is to predict the exact boundary locations, and offsets can be added to its outputs as appropriate via optional settings in the Echofilter API.

Each training input image was normalized independently, based on the distribution of S_v values within the training input. Normalization was performed by subtracting the median over all S_v values, and dividing by a robust estimate of the standard deviation derived from the interdecile range ($\sigma = \text{idr}/2.56$). A small number of NaN values were present in the raw S_v data, and these were set to a value of -3 after the normalization step.

The maximum apparent range of the echogram can in some cases be several times further than the actual depth of the water column. This is because the depth dimension corresponds to the time-of-flight of the signals, the maximum of which is determined by a maximum range parameter chosen by the operator of the echosounder, which may be held the same across many recordings and thus may be much larger than the local depth of the water column. In order to get the most precise output for the entrained-air lines from the trained model, we would like to zoom in on only the salient region of the image: the water column, extending from seafloor to sea surface. This allows the model to predict the boundary point with sufficiently high granularity. However, since the depth of the seafloor is not necessarily known *a priori*, the model needs to be able to determine the depth of the seafloor, or range to sea surface, from the full echogram as well. For testing, we thus use a two-step approach. First, the full echogram is presented to the network and the seafloor and/or surface lines are predicted. These outputs are used to zoom in on the water column. Second, this zoomed-in echogram is presented to the network, and precise seafloor, surface, and entrained-air lines are generated.

Inputs to the network are samples from the distribution of plausible echograms. During training, inputs to the network were drawn from the training partition and augmented with several operations. (i) Temporal stretching, stretch/squashed by a factor sampled log-uniformly from $[0.5, 2]$. (ii) Random depth cropping. With $p = 0.1$, the depth was left at the full, original extent. With $p = 0.1$, the echogram was zoomed in on the range from the shallowest surface depth to the deepest seafloor depth (the “optimal” zoom). With $p = 0.4$, the echogram was zoomed in to a random range of depths close to the optimal zoom, stretched or squashed by up to 25%, but never so much as to remove more than 25% of the the entrained-air line or (for downfacing recordings) more than 50% of the seafloor line. With $p = 0.4$, the echogram was zoomed in to a random range of depths between the full original extent and the “optimal” extent. Depth upper and lower limits were selected uniformly across the appropriate range. (iii) Random reflection in the time (ping) dimension, performed with $p = 0.5$. (iv) “Color” jitter. We applied a “brightness” augmentation by offsetting normalised S_v values by a random additive offset chosen uniformly from $[-0.5, +0.5]$, and a “contrast” augmentation by multiplying normalised S_v values by a random multiplicative factor chosen

uniformly from $[0.7, 1.3]$. The same random offset and factor were used for each pixel in an echogram input. The order of the brightness and contrast augmentations was randomly selected for each input. (v) Elastic grid deformation, performed with $p = 0.5$. Elastic deformation was performed separately in the depth and time dimensions, to create an elastic grid deformation. We chose to deform the dimensions separately, instead of jointly as per a standard elastic deformation where space is stretched/squashed in a 2d manner, because our targets are mostly at the ping level (depth of lines at each ping, whether the ping is passively or actively sampled, etc) and apply to the entire column of data. A standard 2d elastic deformation would break the relationship between our input and target. Performing a joint elastic deformation on the echogram input would make it challenging to relate the input to the targets. We used $\sigma = 8$ in the time dimension, $\sigma = 16$ in the depth dimension, and $\alpha = 0.1$ in both dimensions. The echogram was interpolated in 2d, with the interpolation order randomly selected from linear, quadratic, and cubic (equal weighting).

Finally, the echogram was rescaled to size $(128, 512)$ pixels (time-by-depth) for presentation to the network with nearest-neighbour interpolation.

3.3 Model architecture

The model architecture used is a U-Net (Ronneberger et al., 2015) with EfficientNet MBConv blocks (Howard et al., 2017; Tan and Le, 2019). This architecture is a convolutional neural network (CNN) with residual skip connections across blocks, 6 encoder layers where the size is spatially compressed, 6 decoder layers where the size is expanded back to the original input dimensions, and skip connections from the encoder to decoder blocks. The network has a backbone width of 32 channels throughout, and each MBConv block is inverse residual with an expansion factor of 6 (except the very first block, with has an expansion factor of 1). We used depthwise-separable convolutions with a kernel size of 5, and ReLU activations. We used Squeeze & Excite attention layers (Hu et al., 2019) on each block with a reduction factor of 2.

Since the input is rectangular, with higher resolution in the depth dimension, we downscaled the time dimension at a slower rate than the depth dimension. Downscaling was performed with maxpooling using a kernel size and stride of either 1×2 or 2×2 (alternating blocks). The depth dimension was downscaled after every block, whilst the time dimension was downscaled every other block.

The decoder branch was a mirror of the encoder: upscaling in the depth dimension after every block, and in the time dimension every other block. Upscaling was performed using bilinear interpolation with `torch.nn.Upsample`.

The model has 10 output planes. These correspond to the probability (represented in logit form) that a pixel is at the boundary point for (1) the entrained-air (expanded), (2) the entrained-air (original), (3) the seafloor line (expanded), (4) the seafloor line (original), (5) the surface line; and the probability (logit) that a pixel is within (6) a passive data period, (7) a bad data period (vertical region), (8) a miscellaneous bad data patch (to accompany expanded lines), (9) a miscellaneous bad data patch (to accompany original lines), (10) a miscellaneous bad data patch (to accompany original seafloor/expanded entrained-air).

In practice, the expanded/original lines are almost identical and their pseudo-replication during training was superfluous, but their inclusion did indirectly increase the contribution of the entrained-air and seafloor lines towards the loss term. When performing inference with the model, we discard outputs 2, 4, 9, and 10.

For the Bifacing model, these 9 output planes are replicated three times. One is the standard output, the second are logits which are updated only on downfacing inputs, and the third are logits which are updated only on upfacing inputs. In this way, the model learns to represent conditional probabilities

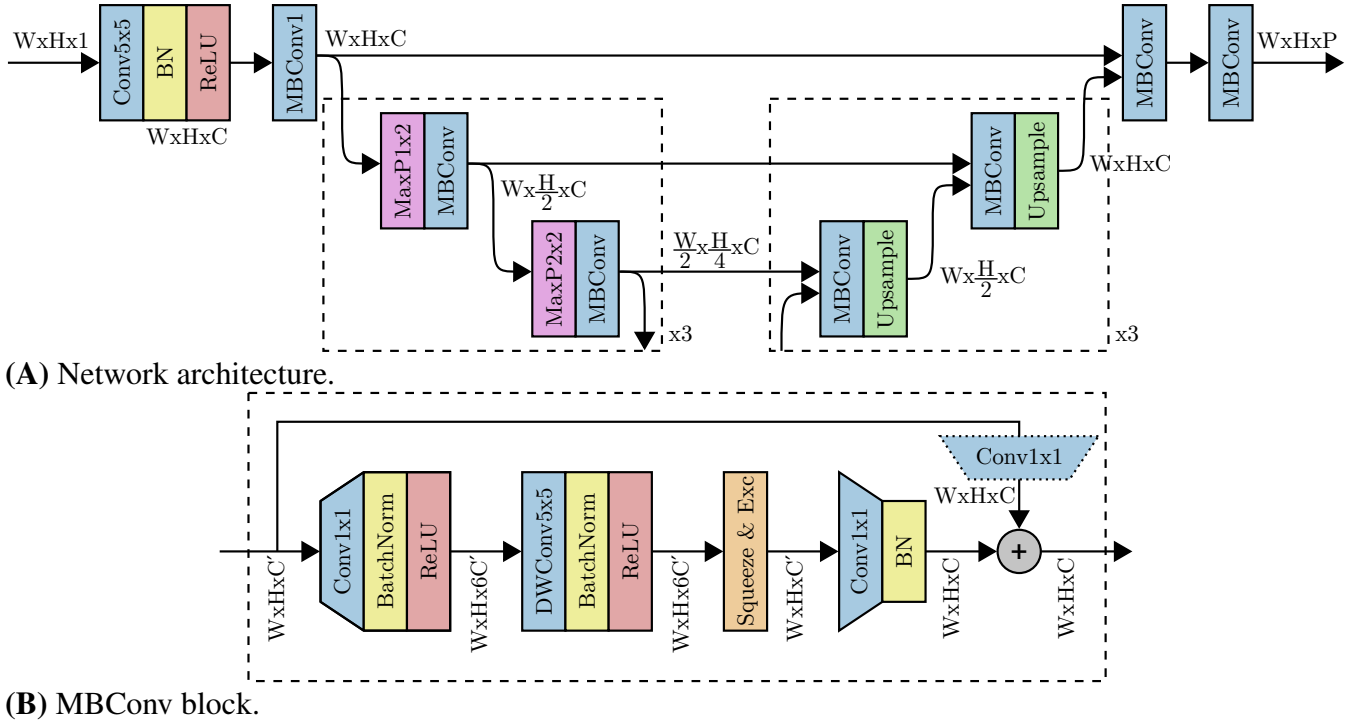


Figure 2 Neural network architecture for the Echofilter model. (A) Main architecture, using an adaptation of the U-Net framework with 6 downsampling blocks, 6 upsampling units, and a single skip connection at each spatial resolution. The network contains a convolutional layer with 5×5 kernel and “same” padding ($\text{Conv}5 \times 5$); BatchNorm (BN); rectified linear unit (ReLU); MBConv blocks (see panel B); max pooling (MaxP), with either 1×2 or 2×2 kernel and stride; and bilinear upscaling (Upsample) layers. The size of the latent representation of the image as it passes through the network is indicated. We train the network with $W = 128$, $H = 512$, $C = 32$. (B) Structure of MBConv block, containing pointwise convolution ($\text{Conv}1 \times 1$), depth-wise convolution ($\text{DWConv}5 \times 5$) and Squeeze & Excite layers. For downscaling blocks $C' = C$, and for upscaling blocks $C' = 2C$. The pointwise convolution on the residual branch is only present for upscaling blocks, where $C' \neq C$.

$P(\text{boundary}|\text{upfacing})$, etc. After training the model, we can ask it to predict the boundaries and masks agnostic of the orientation of the recording, or conditioned on the orientation (upfacing or downfacing).

3.4 Model training

The model was optimized with gradient descent to minimise a loss function. The loss function acts as a proxy for the task of interest; a high loss corresponds to worse performance on the task, and a low loss to better performance. We constructed our loss function as the sum of several terms, each corresponding to one of the output planes produced by the model. The loss terms for the seafloor, sea surface, and entrained-air lines were each the cross-entropy between the column of logits across all depths for a single ping against a one-hot representation of the depth of the line. The loss terms for the passive collection and bad data periods were binary cross-entropy between the model’s output for that ping (a single scalar, after collapsing the depth-dimension with LogAvgExp) and the target value. The loss term for the localised bad data regions was binary cross-entropy. Outlying surface line values detected with our algorithm during preprocessing were masked out from the training objective. We took the mean over pings for all loss terms. We took the mean over the batch dimension; for outputs conditioned on the orientation of the echosounder, we masked out irrelevant samples before taking the batch-wise mean. When training the bifacing model

with conditioning signals, all stimulus presentations were double-counted and the entire loss was divided by two to correct for this.

The model was optimized using the RangerVA optimizer (Wright, 2019), which combines RAdam, Lookahead, with Gradient Centralization (Liu et al., 2020; Zhang et al., 2019; Yong et al., 2020; Tong et al., 2019), with a weight decay of 1×10^{-5} . We used a batch size of 12 samples, and stratified the batches to contain the same ratio of downfacing and upfacing samples as available in the aggregated training set. The learning rate followed a cyclic learning rate schedule (Smith, 2015, 2018; Smith and Topin, 2017). In each cycle, the learning rate warmed up for the first 10% of training, and warmed down for the last 50%. During the LR warmup period, the momentum was decreased from a maximum of $\beta_1 = 0.98$ to a base of $\beta_1 = 0.92$, and then increased back to 0.98 during the LR warmdown period. Both the LR and momentum were increased and decreased with cosine annealing. The second moment parameter was held constant at $\beta_2 = 0.999$ throughout training. In the first cycle, the model was trained for 100 epochs with a maximum learning rate of $LR = 0.012$. In subsequent cycles, the training duration was progressively doubled and maximum learning rate halved. We trained two models: the Bifacing model was trained for three cycles (700 epochs), whilst the Upfacing-only model was trained for two cycles (400 epochs). The model parameters were saved at the end of each cycle for subsequent analysis. We chose to stop the cyclic training process when the model’s validation performance had reached a plateau.

The Upfacing model was trained on MP:sta \uparrow and GP:sta \uparrow datasets, which contain only upfacing S_v recordings. The Bifacing model was trained on the MP:mob \downarrow dataset in addition to the MP:sta \uparrow and GP:sta \uparrow datasets. To address the smaller size of the GP:sta \uparrow dataset, we upsampled it by presenting echograms drawn from it twice per epoch instead of once (for both models).

The model architecture and training hyperparameters were each selected over a series of manual searches against the validation partition with short training durations of 5 or 20 epochs.

The network was trained using PyTorch 1.2.0 and CUDA 10.2. The model training and testing were done on the DeepSense high performance computing cluster with each training cycle or test using a 20 Core IBM Power8NVL 4.0 GHz compute node with 512 GB of RAM and a pair of NVIDIA Tesla P100 GPUs with 16 GB of GPU memory.

The Echofilter model can be trained using the command `echofilter-train`, with training parameters set at the command prompt.

3.5 Model output post-processing

The neural network model is configured to generate predictions for each output type at the pixel level. That is to say, for each pixel in the input echogram, the network predicts a set of output variables at that particular pixel.

For the passive data and bad data periods, we convert this output into a 1d time series by taking the log-avg-exp over the depth dimension (Lowe et al., 2021).

We converted the model’s output into lines as follows. For each boundary line, our model predicts the probability that each pixel is the location of said boundary. We integrated this probability across depth to create a cumulative probability density estimate, and identified the depth at which the cumulative probability exceeded 50%. In so doing, we generate a boundary depth prediction for every ping.

For the purposes of the machine learning model, all salient information needed to produce its outputs is contained in data at, or immediately surrounding, the water column. However, some echosound recordings have much greater range than this, extending out beyond the water column with a large number of samples.

In order to put the echogram into the network, we scale the depth dimension down to 512 pixels. For echograms much larger than the water column, this step incurs a loss of information, since the water column may occupy only a small fraction of the 512 pixel resolution.

In order to alleviate this issue, the echofilter protocol may run the echogram through the network twice, once zoomed out and once zoomed in on the water column. In the first instance, the echogram is “zoomed out” to the maximum extent and scaled down to 512 pixels. The depths of the seafloor or sea surface line is noted (the choice of line depending on echosounder orientation), and used to estimate the extent of the water column. Using a robust estimate of the standard deviation of depths in this line, we set our limit to be 4 standard deviations out from the mean of the line, or the furthest extent of the line, whichever is least distal. For upfacing recordings, we zoom in on the range from the deepest recording up to this depth minus an additional 2 m. For downfacing recordings, we zoom in on the range from the shallowest recording depth down to this depth plus an additional 2 m. After cropping the echogram down to this range of depths, we scale it down to 512 pixels and present it to the network again. The output from the second, “zoomed-in” presentation is used to determine the final entrained-air, surface/seafloor lines and other outputs.

This “zoom+repeat” technique provides gains (see Section 4.1.3), but is needlessly expensive when only a small fraction of the echogram is outside the water column. For this reason, we only perform the second presentation if more than 35% of the echogram would be cropped out. This setting can be controlled with `--autozoom-threshold` argument to Echofilter.

In our analysis, we observed that Echofilter’s bad data predictions were not sufficiently accurate. Furthermore, the mask can include a large number of small disconnected areas, which results in a inconveniently large number of regions to import into Echoview. In order to counter this, we can merge together regions with small gaps in between them, and impose a minimum size threshold on regions to be included in the output. We merged together consecutive passive regions annotations provided by the model with a gap smaller than 10 pings, and similarly for bad-data period labels. Any remaining regions shorter than 10 pings in length were omitted from the final output. For bad data patches, any patch with an area smaller than 25 ping-metres was omitted from the final output. In extremis, we can omit all bad-data annotations from Echofilter’s region outputs.

An alternative solution to noisy outputs is to spatially smooth the output probabilities. We can apply a Gaussian smoothing kernel across each output plane before converting the logits into probabilities, and subsequently into lines and regions. However, we did not find this process led to better results.

Lines and regions produced by Echofilter are exported into Echoview line (EVL) and region (EVR) files so they can be imported into Echoview. Additionally, the Echofilter command line supports saving lines and regions directly into the EV file which it is processing (Windows OS and a licensed copy of Echoview required), removing the subsequent step of manually importing the files.

Inference using a pretrained model can be performed on EV (Windows-only) or CSV files with the command `echofilter`. Pre-processing and post-processing options can configured be set at the command prompt.

4 RESULTS

We evaluated the performance of our models using coarse-grained quantitative metrics (Section 4.1), and also by detailed investigation with qualitative outputs (Section 4.3).

4.1 Quantitative evaluation

We evaluated the overall performance of our final model by comparing the final “good data” mask produced by the model with that of the target labels. The target mask indicates which values within the echogram should be included in biological analyses. This mask excludes all values above the entrained-air line, below the seafloor line, during passive data collection regions, or marked as “bad data”. Our model produces outputs corresponding to each of these elements, resulting in a corresponding mask. We measured the alignment between the two masks using the Jaccard index, described in Section 4.1.1.

For our purposes, the most important output from the Echofilter model was the entrained-air line, which provides segmentation between the air bubbles entrained into the water column, and the rest of the water column. To provide a human-interpretable measurement of the error in the placement of this line, we measured the mean-absolute-error (MAE) between the depth of model’s entrained-air line and the target target. See Section 4.1.2 for more details.

Other outputs from the model were evaluated similarly, using either the Jaccard index, or the MAE, or both.

In all cases, we show the performance of the model on the test partition, which was held out during all stages of model development and training. For the MP:mob↓ dataset, test recordings were taken from survey transects which were held out in their entirety, hence this testing is performed on novel locations which the model has not seen before.

4.1.1 Jaccard Index

The model’s output was principally evaluated using the Jaccard index metric (Jaccard, 1912), also known as Jaccard similarity coefficient score, and intersection-over-union score (IoU). This metric is commonly used to evaluate the performance of image segmentation models within the field of Computer Vision. The Jaccard index of two masks is calculated by assessing their overlap; it is the ratio of the size of the intersection of the two masks against their union (see Equation 1). For this study, one mask identifies the data marked as “good” by a human annotator, and the other mask is the data marked as “good” by the model. A higher Jaccard index is better, indicating the two masks are better aligned. We chose to use this performance metric because it is robust against padding the input with additional signal range outside of the water column (below the seafloor for downfacing recordings, or above the sea surface for upfacing recordings).

$$J(\text{annotated}, \text{predicted}) = \frac{\text{Area}(\text{annotated} \cap \text{predicted})}{\text{Area}(\text{annotated} \cup \text{predicted})} \quad (1)$$

For each the MP:sta↑ and GP:sta↑ datasets, the Jaccard index measurements we report are measured as the total area of the mask intersections across the whole test set, divided by the total area of the union of the two masks (i.e. the division operation performed after the summation). For the MP:mob↓ dataset, the Jaccard index reported is the average Jaccard index over all the EV files in the test set (i.e. the division operation performed before the mean). In both cases, we determine measure the standard error (SEM) by considering the distribution of Jaccard indexes over EV files. For any recording where the target mask is all marked as False (no good data), the intersection of the predicted area with the target area is always 0, and any prediction from the model results in a anomalously minimal score. Consequently, we excluded examples where the target was an empty mask when measuring the SEM.

4.1.2 Mean Absolute Error

We performed further evaluation of the model’s outputs using the mean absolute error (MAE) performance metric (Equation 2). We applied the MAE to measure the quality of the output lines. In this context, the MAE corresponds to the average distance (across pings) of the model’s line from the target line. A lower MAE is better, indicating the model’s line is (on average) closer to the target line.

$$\text{MAE} = \frac{\sum_i |y_i - \hat{y}_i|}{n} \quad (2)$$

When measuring the MAE of the lines, we excluded pings which were marked as being within a passive or removed data region in the target annotations. To find the overall MAE, we took a weighted mean over all files, using the number of pings used to measure the MAE in that file as its weighting. Additionally, we report the standard error measured across the files (without weighting for number of pings).

4.1.3 Impact of post-processing steps

We evaluated the performance of the final Upfacing and Bifacing models before and after each post-processing step impact described in Section 3.5. Our results are shown in Table 2.

We found that the two models gave similar performance on the stationary-upfacing datasets, with an average error in entrained-air line placement of around 1 m on the Minas Passage dataset (MP:sta \uparrow), and 0.6 m on the Grand Passage dataset (GP:sta \uparrow); and an overall Jaccard index of 95% and 88% respectively. We note that the range of the Minas Passage stationary data is restricted to the water column, whereas Grand Passage data recordings have a range several times the depth of the water column. Consequently, using our two step “zoom+repeat” stimulus presentation provided a notable increase in performance of the models on the GP:sta \uparrow data, but not on MP:sta \uparrow . The Bifacing model was also applied on the downfacing (MP:mob \downarrow); these recordings also have larger range than the extent of the water column and a notable improvement was seen by performing the zoom+repeat process. We found that using a threshold of 0.35 to determine when to do the zoom+repeat step resulted in slightly, but not statistically significant, worse performance on the MP:sta \uparrow dataset, and no change on MP:mob \downarrow and GP:sta \uparrow . This suggests that zoom+repeat should ideally always be performed, but notable processing time savings can be made with minimal impact on the output when using the threshold method.

The remaining optional post-processing steps were considered with thresholded zoom+repeat in place. We found no significant differences when small regions were merged together or dropped from the output. Omitting bad data regions and patches entirely had a positive impact on the overall performance on the GP:sta \uparrow data, but a negative impact on MP:sta \uparrow data. There was no impact on MP:mob \downarrow data because the model did not predict any bad data regions on this test dataset.

We considered the effect of logit smoothing on the model’s final output by applying this postprocessing step, in addition to thresholded zoom+repeat and ignoring all removed bad annotations, with a Gaussian kernel size of 1. We found that logit smoothing had a negative impact on the accuracy of the entrained-air line placement, and on the overall mask output.

Our results indicate the Bifacing model performed better on the mobile-downfacing dataset (MP:mob \downarrow) than either of the stationary-upfacing datasets, despite having more stationary-upfacing training data than mobile-downfacing data.

Table 2 Impact of post-processing steps on the model performance metrics. (The entry “Bifacing -conditioning” includes the steps “thresholded z+r” and “ignore small regions”.)

Model	Overall Jaccard Index (%)			Entrained-air MAE (m)		
	MP:mob↓	MP:sta↑	GP:sta↑	MP:mob↓	MP:sta↑	GP:sta↑
Upfacing w/o zoom	–	95.06±0.34	88.06±3.88	–	0.99±0.04	0.63±0.08
+ zoom+repeat	–	95.11 ±0.35	92.09±1.01	–	0.95 ±0.04	0.57 ±0.07
w/ thresholded z+r	–	95.09±0.34	92.07±1.01	–	0.98±0.04	0.58±0.07
+ ignore small regions	–	95.08±0.34	92.10±1.00	–	0.98±0.04	0.58±0.07
+ ignore all “removed”	–	94.77±0.44	93.01 ±0.76	–	0.98±0.04	0.58±0.07
+ logit smoothing	–	94.27±0.46	92.48±0.86	–	1.10±0.05	0.62±0.09
Bifacing w/o zoom	98.22±0.09	94.90±0.35	88.35±3.93	0.40±0.03	1.00±0.05	0.59±0.05
+ zoom+repeat	98.80 ±0.10	94.86±0.40	92.95±1.01	0.32 ±0.03	0.98 ±0.04	0.53 ±0.03
w/ thresholded z+r	98.79±0.10	94.90±0.35	92.95±1.01	0.32 ±0.03	1.01±0.05	0.53 ±0.03
+ ignore small regions	98.79±0.10	94.91 ±0.35	92.97±1.00	0.32 ±0.03	1.01±0.05	0.53 ±0.03
+ ignore all “removed”	98.79±0.10	94.74±0.42	93.45 ±0.64	0.32 ±0.03	1.01±0.05	0.53 ±0.03
+ logit smoothing	98.60±0.10	94.35±0.43	93.12±0.67	0.38±0.03	1.10±0.05	0.57±0.05
Bifacing -conditioning	98.78±0.10	94.90±0.35	92.98±0.99	0.32 ±0.03	1.01±0.05	0.53±0.03

4.1.4 Impact of model training duration

We investigated the impact of training time on the final model outputs. We comparing the output of each of the models at the end of each stage of the cyclic training process. For this analysis, we used thresholded zoom+repeat, and merged/ignored small regions in the model output.

As shown in Table 3, we found that further training cycles improved the performance on MP:sta↑ and MP:mob↓, though with diminishing returns, but *reduced* the performance on GP:sta↑.

Table 3 Performance of models after each training cycle (different total training durations).

Model		Overall Jaccard Index (%)			Entrained-air MAE (m)		
		MP:mob↓	MP:sta↑	GP:sta↑	MP:mob↓	MP:sta↑	GP:sta↑
Upfacing	100ep	–	95.05±0.33	93.32±0.87	–	1.00±0.05	0.52±0.03
	400ep	–	95.08 ±0.34	92.10±1.00	–	0.98 ±0.04	0.58±0.07
Bifacing	100ep	98.50±0.11	94.93±0.32	93.52 ±0.69	0.37±0.03	1.04±0.05	0.51 ±0.03
	400ep	98.75±0.09	94.97±0.33	93.18±0.92	0.33±0.03	1.02±0.05	0.52±0.03
	700ep	98.79 ±0.10	94.91±0.35	92.97±1.00	0.32 ±0.03	1.01±0.05	0.53±0.03

4.1.5 Performance break-down across outputs

Our results so far have focused on the quality of the overall mask yielded by the Echofilter model, and the distance of the entrained-air line from its target depth only. Further to this, we investigated the performance of each of the outputs produced by the model individually.

We considered the Jaccard index for each output. For the entrained-air line, the Jaccard index measurement considers the area beneath the entrained-air line — for upfacing recordings, this extends to the echosounder and for downfacing recordings it extends to the true seafloor line (as provided by the expert’s annotation). Similarly the Jaccard index for the surface line extends from the surface to the echosounder, and is only measured for upfacing recordings. For the seafloor line, we compare the area from the seafloor line to the echosounder. For passive data region annotations, we compare the set of pings identified as passive by the

model with the target annotations, performing a 1d Jaccard index calculation. The vertical removed data regions are measured in the same way as the passive data region annotations, using a 1d Jaccard index. The Jaccard index for the bad data patches is a comparison of the area marked as bad data by the model with a target mask indicating the locations of bad data patches.

We measured the MAE of the surface and seafloor lines in the same way as for the entrained-air line (see Section 4.1.2). Additionally, we measured the root-mean-square error (RMSE) in a similar manner to the MAE. In this case, we found the average MSE across all the samples in the dataset, and then took the square root after averaging.

Table 4 Final model performance for each output type. The performance of the Upfacing (@400 epoch) and Bifacing (@700 epoch), with thresholded zoom+repeat, merging/ignoring small output regions.

Output	Upfacing		Bifacing		
	MP:sta \uparrow	GP:sta \uparrow	MP:mob \downarrow	MP:sta \uparrow	GP:sta \uparrow
Jaccard Index (%; larger is better)					
Overall	95.13 \pm 0.33	92.10 \pm 1.00	98.79 \pm 0.10	94.91 \pm 0.35	92.97 \pm 1.00
Entrained-air	96.05 \pm 0.29	94.49 \pm 0.50	99.13 \pm 0.08	95.96 \pm 0.28	94.95 \pm 0.29
Surface	98.87 \pm 0.75	92.45 \pm 4.19	–	98.87 \pm 0.75	98.10 \pm 1.32
Seafloor	–	–	99.70 \pm 0.03	–	–
Air–Seafloor	–	–	98.81 \pm 0.09	–	–
Passive	100.00 \pm 0.00	99.97 \pm 0.01	99.83 \pm 0.05	100.00 \pm 0.00	100.00 \pm 0.00
Removed (vertical region)	40.58 \pm 3.96	24.68 \pm 7.65	0.00 \pm 0.00	38.92 \pm 4.19	25.78 \pm 8.07
Patch (anomalous bad data)	0.16 \pm 0.07	0.20 \pm 0.07	0.00 \pm 0.00	0.30 \pm 0.11	0.20 \pm 0.07
Mean Average Error (m; smaller is better)					
Entrained-air	0.98 \pm 0.04	0.58 \pm 0.07	0.32 \pm 0.03	1.01 \pm 0.05	0.53 \pm 0.03
Surface	0.42 \pm 0.27	1.36 \pm 1.08	–	0.42 \pm 0.27	0.25 \pm 0.18
Seafloor	–	–	0.13 \pm 0.01	–	–
Root-Mean-Square Error (m; smaller is better)					
Entrained-air	2.18 \pm 0.08	1.24 \pm 0.14	0.89 \pm 0.06	2.23 \pm 0.09	1.10 \pm 0.06
Surface	2.84 \pm 0.32	7.63 \pm 2.35	–	2.87 \pm 0.32	2.64 \pm 0.81
Seafloor	–	–	0.45 \pm 0.02	–	–

As shown in Table 4, we found that the Bifacing model placed the seafloor line with very low error (only 0.14 m on average) on the MP:mob \downarrow test set. Both models placed the surface line with low error (0.42 m) on the MP:sta \uparrow dataset. The Bifacing model was more accurate on GP:sta \uparrow (0.25 m average error), whereas the Upfacing model was less accurate (1.36 m average error). Manual inspection of the results demonstrates that the Upfacing model is sometimes confused by reflections in the additional range of these recordings, whilst the Bifacing model was not confused by these reflections.

The passive region annotations are highly accurate, reaching 100% accuracy on MP:sta \uparrow and GP:sta \uparrow . On the MP:mob \downarrow dataset, the Bifacing model attains a Jaccard index of 99.83%.

The removed data region annotations were challenging for the model to replicate, attaining a Jaccard index of only 40% on MP:sta \uparrow and 25% on GP:sta \uparrow . The anomalous bad data patches were impossible for the network to learn with any meaningful reliability, with a Jaccard index of $\leq 0.3\%$. The poor performance of both of these annotations yields an increase in performance when small outputs are ignored (as seen in

Section 4.1.3). On GP:sta \uparrow , the removed-data vertical region annotations are sufficiently poor to yield an increase in performance when they are dropped entirely (see Section 4.1.3).

4.2 Inter-annotator Agreement Benchmarking

For the task of annotating the data with segmentation lines, we do not have access to ground-truth labels. The extent to which air is entrained in the water column is not observed directly, and can only be estimated based on the echosounder recordings. With training and experience, human annotators can learn which datapoints correspond to entrained-air and which to fish populations within the water column. However, without a ground truth measurement, the annotations are subjective and will differ between annotators.

With this in mind, it is difficult to know how well we could expect the model to perform at the task. Though the Bayes error rate is not known, we do know it is infeasible to expect perfect agreement between the model and the human annotations, since human annotators do not always agree amongst each other and are not necessarily consistent in their choice of line placement. We endeavoured to quantify how well our model performs by measuring the agreement between two human annotators to act as a baseline.

Table 5 Comparison of agreement between several annotation sources. We compared several annotation methods against expert labels created by JD. The Jaccard Index over all recordings is shown, in addition to the mean absolute error (MAE) and root-mean-square error (RMSE) for the placement of the entrained-air separation line ($n = 10$, \pm inter-recording standard error). Note that JD used Echoview to generate seed annotations for refinement into finalised annotations.

Annotator	Jaccard Index (% , larger is better)				Δ Entrained-air (m)	
	Overall	Entrained-air	Removed	Patch	MAE	RMSE
Human expert (LPM)	90.65 \pm 1.15	92.38 \pm 0.93	97.76 \pm 3.93	0.29 \pm 0.10	0.86 \pm 0.10	1.63 \pm 0.17
Echoview	88.67 \pm 8.45	90.89 \pm 1.13	31.31 \pm 20.25	–	1.05 \pm 0.12	2.01 \pm 0.19
Echofilter: Upfacing	90.46 \pm 8.80	93.16 \pm 0.91	70.72 \pm 23.84	0.32 \pm 0.09	0.76 \pm 0.05	1.25 \pm 0.11
Echofilter: Bifacing	91.31 \pm 8.65	92.97 \pm 0.97	92.84 \pm 5.05	0.38 \pm 0.11	0.78 \pm 0.04	1.27 \pm 0.09

We selected 10 EV files from the Grand Passage stationary-upfacing dataset (GP:sta \uparrow). These files were selected because they had not yet been post-processed by either annotator. The goal was to generate the annotations without bias from previous experience with the individual files by either annotator. In addition, we ensured that the selected files were composed of sufficiently complex data so that any differences in line placement between each annotator would be highlighted. Annotations were generated by Echoview using the pre-existing workflow (Figure 9, left panel). These seed annotations were used by JD and LPM in order to independently create two sets of finalised annotations for all 10 files. We then created annotations using Echofilter (models Upfacing@400ep and Bifacing@700ep, using thresholded zoom+repeat, and dropping small regions). While both annotators are experts in this field, JD was the most experienced at handling this data — her annotations constituted the majority of the annotations used to train the models. Consequently, we treated JD’s annotations as the ground truth labels, and measured the performance of the other annotation methods in comparison to her labels.

We found that the level of agreement in placement of the entrained-air line between Echofilter and JD exceeded that of LPM, with higher Jaccard Index and a smaller average distance between the line depths (see Table 5). This suggests our results are near to human-level performance.

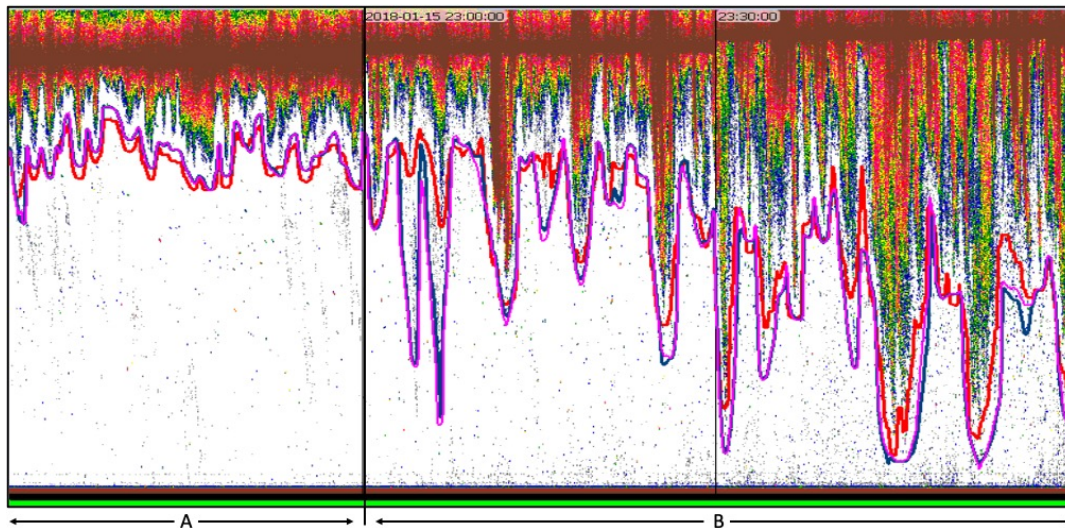


Figure 3 Entrained air lines as defined by Echofilter (Bifacing@100ep: blue; Upfacing@100ep: pink) and by Echoview (red). (A) A 5-minute data collection period during which entrained air does not penetrate deeply into the water. The Echoview line is further from the entrained air than the Echofilter lines, leaving greater amounts of white space and thereby unnecessarily excluding more water column from analyses. (B) Two 5-minute data collections periods during which the returns from entrained air are more depth dynamic. The Echofilter placement of the entrained air lines more closely reflect the penetration of the entrained air in terms of depth and width. In the horizontal dimension, the Echofilter lines are appropriately placed further from the entrained air in the particularly steep sections. Note that Echofilter entrained air lines as defined by each model (Bifacing@100ep and Upfacing@100ep) are essentially equivalent although not identical.

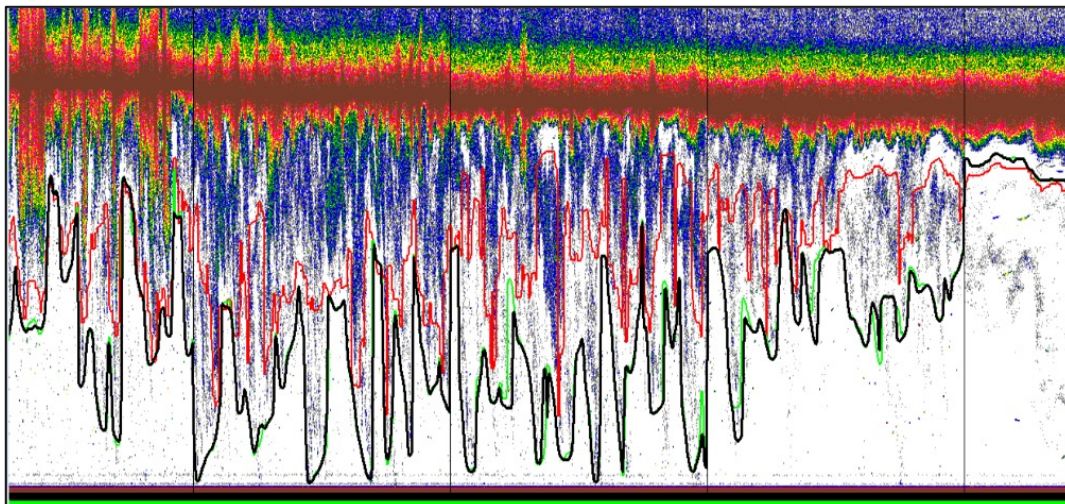


Figure 4 Echogram demonstrating that although not identical, the entrained air line as calculated by the two Echofilter models (Bifacing@100ep: green; Upfacing@100ep: black) is a pronounced improvement over that produced by Echoview (red line).

4.3 Manual evaluation of model outputs

Manual investigation of the Echofilter results were carried out by JD and LPM on a Windows 10 operating system, using Echoview 10 or Echoview 11, newly released at the time of testing. The performance of Echofilter was evaluated on 24 Echoview files, selected from the test partition as described in Section 2.

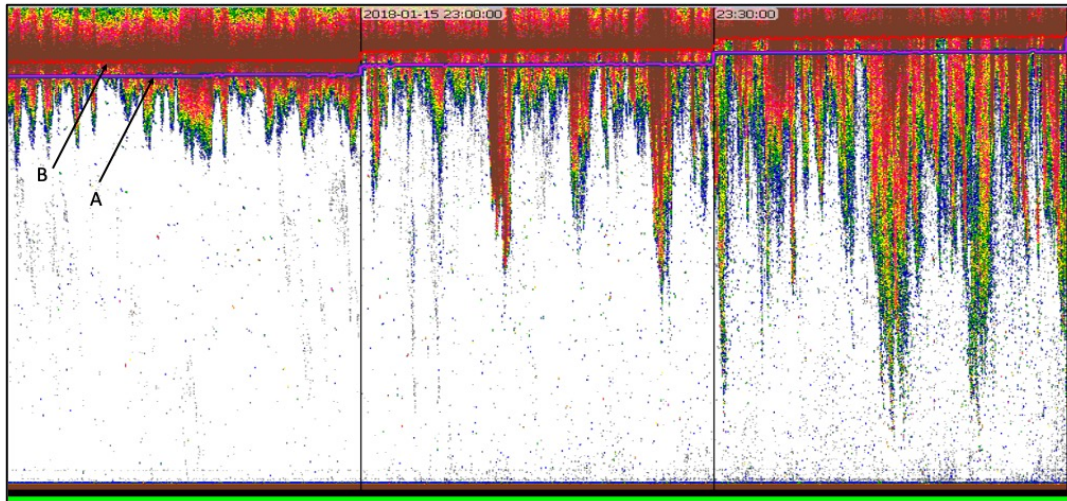


Figure 5 (A) Example showing appropriate and adequate placement of the surface line by Echofilter models: Bifacing@100ep (blue) and Upfacing@100ep (pink). The line placements include the 1-m offset required to eliminate bias from acoustic beam deadzone. (B) For reference, the surface line placement at the surface as defined by Echoview.

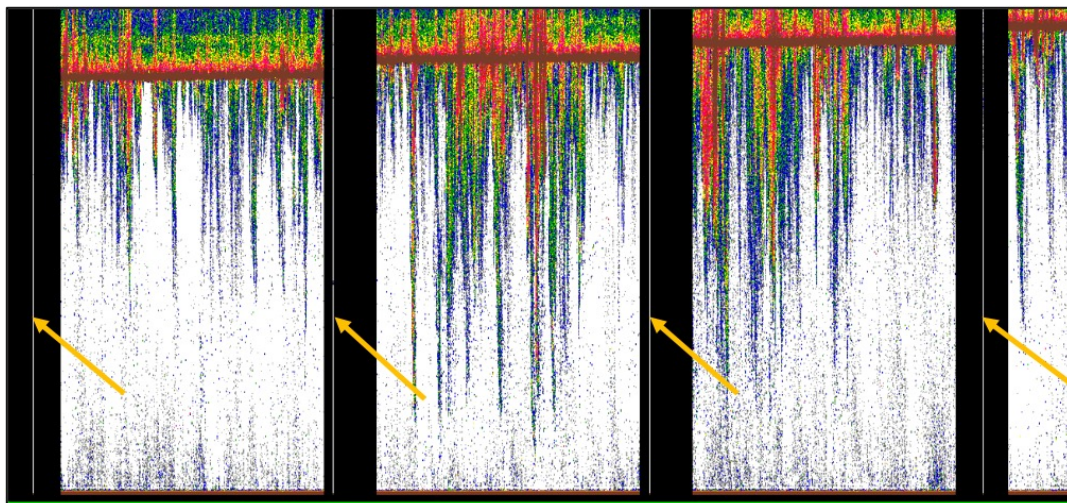


Figure 6 Passive data regions (black vertical bars) as identified by Echoview algorithms. Note the white vertical lines marked by yellow arrows within the black passive data regions. The white vertical lines are single pings or a few pings misclassified by the Echoview algorithm. During testing no such occurrences were noted in the Echofilter results.

During model development, a series of iterative testing and upgrades to Echofilter was undertaken. Echofilter was run on the entire set of test files, applying both models (Bifacing and Upfacing, with thresholded zoom+repeat, and logit-smoothing) to the data for comparative purposes. The results were examined for adequacy and appropriateness of the placement of lines (sea surface or seafloor, entrained air, and nearfield), the identification of the passive data collection periods and identification of bad data regions. Issues with the outputs were investigated in detail, and used to make changes to the model architecture design, training paradigm, or to the format of input and target data provided to the model during training. This process was iterated until any additional improvements were marginal and inconsequential.

By the end of testing and upgrades to the models, both models (Bifacing@100ep and Upfacing@100ep) produced appropriate automated initial placement of the boundary lines. Most importantly, the model

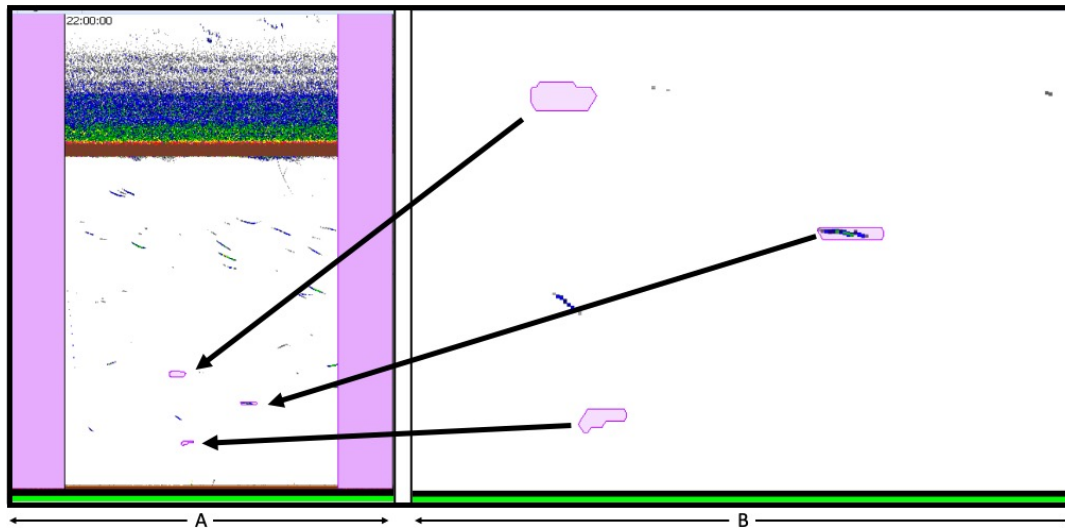


Figure 7 Example of false positive “patch” bad data regions identified by Echofilter. At left is a 5-minute section of echogram with passive data regions (pink rectangles) on either side. At right, enlargement to show the contents within each patch. Empty patches are false positive. The patch containing color samples within it would be classified as fish by the hydroacoustic analyst. It was likely identified as a bad data region by Echofilter because of its nearly horizontal position. The data on which the models were trained contain occurrences of unidentified interference which appear as horizontal lines. Those were classified as bad data regions by the analyst prior to training. Both models (Bifacing@100ep and Upfacing@100ep) designate true and false positives, but differently. Bifacing@100ep results appear to include fewer false positives.

placement of entrained-air boundary lines were visibly superior to the line placements as produced by the Echoview algorithms. The model results proved to be much more responsive than the Echoview algorithms to the entrained air ambit characteristics across the varying tidal flow rates, as shown in Figure 3. In some cases, the automated prediction of the entrained-air line placement as produced by Echofilter were far superior to that produced by Echoview (Figure 4). Note that Echofilter entrained air lines as defined by each model (Bifacing@100ep and Upfacing@100ep) were essentially equivalent, although not identical.

The Echofilter models produced appropriate and adequate automated placement of the surface line, including a user-defined offset; in this case 1 m (Figure 5). Likewise, the Echofilter models produced appropriate and adequate identification of the passive data regions that will be excluded from biological analyses. We found the Echofilter passive data region identification was superior to the Echoview algorithms implemented to automate the identification of passive data regions. The Echoview algorithms would, not uncommonly, exclude a ping or few pings from within the passive data region, thereby inappropriately designating those pings for inclusion in biological analyses, as shown in Figure 6.

In addition to the passive data regions, there are two additional types of bad data regions that are not uncommon to echosounder data. The first type, a “patch” of bad data can be characterized as forming randomly shaped discrete patches. Within the original test segment of 24 files, only three had occurrences of the patch-type bad data region. Two additional EV files containing patch-type bad data regions were identified from the validation and training segments for manual inspection of the patch-type results only. Both Echofilter models performed poorly, generating false positives (Figure 7).

The second type of bad data region is a contiguous time period marked to be removed from analysis. As shown in Figure 8, these bad data regions are identified by Echofilter when the position of the entrained air line resolves to a position intersecting or extending below the bottom line, whether that line is the seafloor

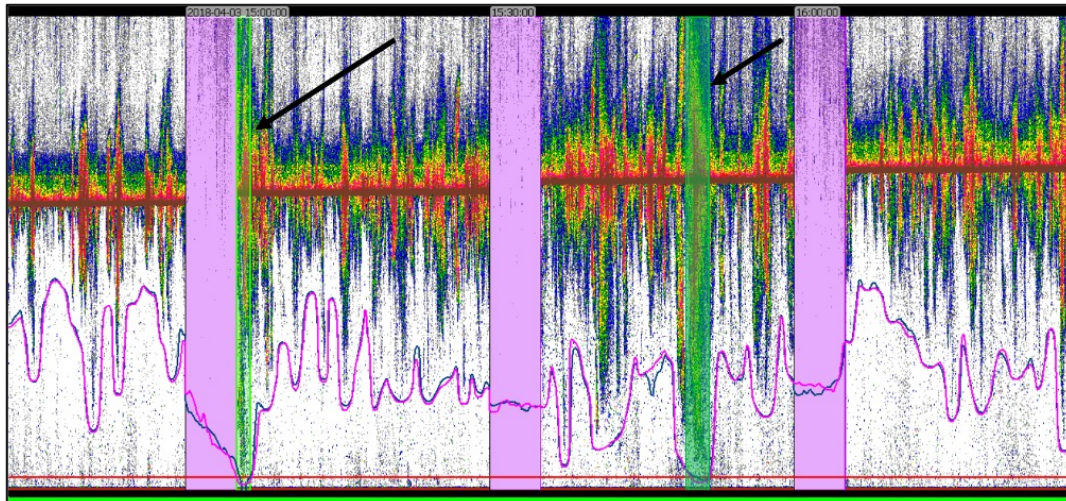


Figure 8 Example of bad data lengths defined by Echofilter (green bars). Bad data lengths are designated when the turbulence line defined by Echofilter (pink or blue in this example) intersects with the bottom analytical line (in this case the line designating the outer boundary of the transducer nearfield). Although these cases meet the criteria, in each case the hydroacoustic analyst would designate the entire recording period as a bad data region due to the strength, penetration, and persistence of entrained air signals through to the nearfield line. No false negatives have been noted except for those recording periods where the whole recording periods should be excluded.

or the line designating the transducer nearfield exclusion line. In other words, when the position of the entrained air line indicates that the entrained air has penetrated the entire depth of the water column. Such occurrences are not uncommon in the Minas Passage and Grand Passage datasets, sometimes occurring for just a few pings and other times the penetration occurs throughout an entire 5-minute data collection period. The single criteria of intersecting or penetrating below the bottom line is insufficient for defining all pings that should be excluded in their entirety. Figure 8 provides an example of just such a case: less than 50% of the water column remains after the entrained air exclusion. In that case, if the goal of the analyses is to understand metrics within the full water column, that data collection period would need to be excluded in its entirety.

4.4 Time-savings analysis

We sought to evaluate the amount of time-savings that the Echofilter model would offer, relative to the existing workflow using Echoview algorithms. Five of the Echoview files from the MP:sta↑ test partition were selected for a time test. The files were selected to represent each tide and phase combination: flooding spring tide, ebbing spring tide, flooding neap tide, and ebbing neap tide, plus one file with especially noisy data for which neither Echoview or Echofilter would likely render a well-placed entrained air line. Annotations were initialised twice: once using the pre-existing workflow utilising Echoview algorithms Figure 9, and once using Echofilter with the Upfacing@100ep model, with logit-smoothing enabled. The entrained-air line in each of the five files was edited by the hydroacoustic analyst (JD) while running a screen-record to record the actions taken and the amount of time required to complete the edits for each entrained-air line. We randomised the order in which tasks (file and seed annotation source) were completed, except the “especially noisy file” which was edited at the end.

Our results, shown in Table 6, demonstrate that using the annotations generated by Echofilter results in less time taken for the human annotator to complete their task. The time taken to finalise annotations

Table 6 Results from the time-to-edit experiment. A hydroacoustician used the entrained-air lines produced by either Echoview or Echofilter to seed their annotations. We compare the amount of time needed to convert the seed lines into our “ground truth” annotation lines.

Tide & Phase	Edit order		Edit time (MM:SS; ↓)		Reduction (↑)
	Echoview	Echofilter	Echoview	Echofilter	
Spring Flood	2	6	8:06	4:04	50%
Spring Ebb	3	4	8:00	4:04	49%
Neap Flood	8	7	8:18	4:30	46%
Neap Ebb	1	5	7:08	3:57	45%
Mean			7:53	4:09	47%
Bad file	9	10	4:28	1:51	59%
Overall Mean			7:12	3:42	49%

was consistently 45%–50% shorter when using annotations produced by Echofilter as the seed instead of annotations produced by Echoview, and 59% shorter for the especially noisy file.

4.5 Comparison of dataflows

Echoview software is the international standard for advanced visualization and post-processing of hydroacoustic data. The Echoview dataflow (Figure 9) provides a centralized location to manage the variables and other objects used for post-processing, visualizing and segmenting echosounder data. The dataflow diagram visualizes the post-processing workflow, and can become quite complex. Because the software is highly configurable with a wide selection of parameterized data manipulators it is often possible to find a way to accomplish data processing needs for which Echoview was not originally intended, such as automating a reasonable initial placement of the entrained air line. The two dataflows displayed in the figure demonstrate the complexity of manipulations required when using Echoview to automate the placement of the three lines required to define the analytical region within an EV file versus the highly simplified version accomplishing the same goal but without the complexity.

5 DISCUSSION

5.1 Impact of Echofilter model

We have described the implementation of a deep learning model, Echofilter, which can be used to generate annotations to segment entrained-air appearing in hydroacoustic recordings at tidal energy sites. The goal of this project was to produce an automated, model-based approach to the placement of a line appropriately defining the boundary between that portion of the water column contaminated by acoustic returns from entrained air, and that portion of the water column appropriate for biological analyses. Our motivation was fed by recognition of the urgency with which we must come to a more informed understanding of the inner Bay of Fundy ecosystem in order to assist regulators, developers, stakeholders, and communities in understanding the potential impacts brought by the placement of tidal energy devices in the marine habitat.

Of particular note is that the original goal of the project was fulfilled: the placement of the entrained-air line showed pronounced and measurable improvement over that achieved by Echoview. The testing results demonstrated that the Bifacing and Upfacing models appropriate to the stationary, upfacing data, produce automated line and passive region placement superior to those produced by Echoview. As such, Echofilter provides a complete, improved, automated line placement and passive data region methodology for the stationary, upfacing data collected in Minas Passage.

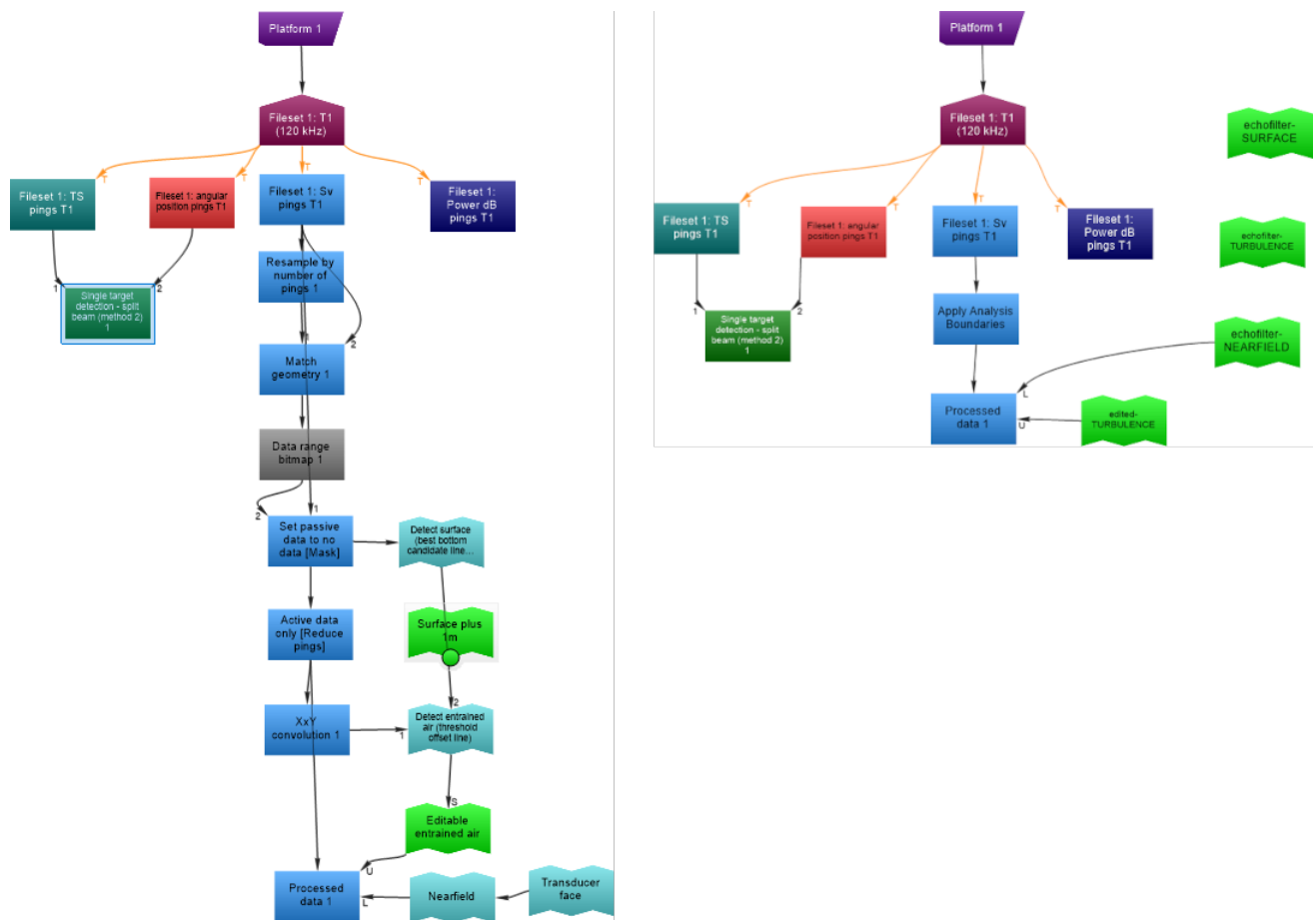


Figure 9 Comparison of the Echoview dataflow template with and without Echofilter. **Left:** An Echoview-only solution. **Right:** An Echofilter solution producing the same line elements within the EV file but with the better placement made by Echofilter. Note the highly simplified Echoview dataflow when Echofilter is implemented. The three green boxes stacked on the right of the figure constitute the three line definitions generated by Echofilter and imported into the Echoview file: surface, entrained air, and nearfield. The fourth green box at the bottom is a copy of the Echofilter-generated entrained air line which allows the analyst to modify the placement of the entrained air line without destruction of the line as generated by Echofilter.

Throughout the development of this project, it became clear that the benefits provided by the outcome go far beyond decreasing the amount of time required to post-process echosounder data. The three main benefits of having undertaken this project are i) the notable increase in efficiency with which the lines can be modified to a final position, ii) the potential for increased internal consistency and consistency among analysts, and iii) the implementation of the production of the full suite required to segment the echosounder data between those produced by physical boundaries versus those returns generated by fish or other marine life: the bounding lines and the passive data collection regions.

The driving factor allowing for the increased efficiency with which hydroacoustic data can be post-processed is that the models are sensitive to the fine-scale nuances in the boundary position of the entrained air. Because of the nuanced placement of the entrained air boundary line, the edits to lines generated by the models tend to be coarse-scale edits (e.g., a ready click or two) rather than the time consuming fine-scale edits required with Echoview line placement. The coarse-scale edits in turn lead to far less analyst fatigue, thereby allowing the analyst to bring the full-force of their intellect, training, and analytical skills to modifying placement of the line segments. Additionally, the reduction in the sheer number of

fine-scale edits provides the opportunity for an increase in the standardization and repeatability of line placement, within an analyst's work and among analysts. These benefits accrue, compounding the initial premium of reducing the analyst's post-processing time commitment by approximately 50%.

The enhancements identified and implemented throughout the testing phase markedly improved Echofilter's features, usability, and customizability. The target for Echofilter was originally to generate the entrained-air line, but once it became clear that Echofilter would become an entire set of external processing in order to generate one line within an Echoview file, resources were invested in producing a full-functional product with sufficient customizability and the capacity to automate the import of the newly generated lines and passive regions back into Echoview shifted the implementation of Echofilter to a genuine value-added product. The ability to run Echofilter in batch mode using a Windows script further enhances its utility because with a few simple commands, the Echofilter tasks can be run overnight.

Machine learning applied to the hydroacoustic data by which we quantify fish distribution and abundance has garnered improvements to the work flow and the efficiency of the work flow that haven't been achieved any other way. The machine learning contribution to assessing the ecological impacts of introducing marine renewable energy devices into the marine habitat is the improved analytical consistency and substantial improvements in the timeliness of analyses and subsequent reporting.

5.2 Limitations Associated with Echofilter

We developed Echofilter with the goal of increasing the efficiency and standardization of the post-processing of hydroacoustic data collected in dynamic marine environments like tidal channels. The model thoroughly evaluated on data recorded from upward facing stationary echosounders at two tidal energy demonstration sites in the Bay of Fundy. The models have not been tested on data collected in other regions, with other instrumentation, or in other deployment configurations. Consequently, the performance of Echofilter on data collected under conditions that differ substantially from those used for model development may be heavily impacted and require some level of re-training to ensure accurate results, which is a non-trivial procedure.

In addition to the entrained air boundary line, Echofilter predicts the depths of the surface (for upfacing recordings) and the seafloor (downfacing). Our performance metrics indicate that these lines are all placed accurately, however we have not thoroughly inspected the model's output on downfacing recordings and can not confirm the integrity of the seafloor line.

In addition to the lines, our model attempts to predict regions which should be excluded from biological analyses. However, it was not possible for the model to learn these annotations with sufficient accuracy to be usable for downstream tasks. Consequently, it is not possible to automate away a need for manual inspection of the data. A hydroacoustician must always inspect the recordings themselves in order to annotate regions to exclude from analysis, and adjust the entrained-air lines as necessary.

5.3 Accessing Echofilter

To ensure the broader community can utilise our model described in this paper, we have released the final implementation, Echofilter, under the AGPLv3 license. Python source code and a stand-alone Windows executable are available at <https://github.com/DeepSenseCA/echofilter>. Additionally, the command line interface (CLI) and application programming interface (API) documentation is available at <https://DeepSenseCA.github.io/echofilter/>.

We hope this tool will prove useful to tidal energy researchers, and the wider hydroacoustic community.

CONFLICT OF INTEREST STATEMENT

The authors declare that the research was conducted in the absence of any commercial or financial relationships that could be construed as a potential conflict of interest.

AUTHOR CONTRIBUTIONS

Manuscript written by SCL and LPM. Data conversion was performed by SCL and JN. Model architecture design and training performed by SCL. Interface and API development by SCL. Model evaluation was performed by LPM and JD. Identification of features of specific value to the hydroacoustics community was performed by LPM. Project oversight by CW, DJH, and SO.

FUNDING

SCL was funded by Mitacs award IT16140. LPM was supported by the Offshore Energy Research Association of Nova Scotia under the Pathway Program.

ACKNOWLEDGMENTS

This work was supported in part by support provided by Mitacs through the Mitacs Accelerate program, and by Offshore Energy Research Association (OERA; <https://oera.ca/>). Computations were performed on the DeepSense (<https://deepsense.ca/>) high-performance computing platform. DeepSense is funded by ACOA, the Province of Nova Scotia, the Centre for Ocean Ventures and Entrepreneurship (COVE), IBM Canada Ltd., and the Ocean Frontier Institute (OFI). We thank Echoview Software Pty Ltd. and Haley Viehman, Ph.D. for providing support and technical advice for this project.

REFERENCES

- AECOM Canada Ltd (2009). Environmental assessment registration document - Fundy Tidal Energy Demonstration project volume 1: Environmental assessment. *Project Number 107405*.
- Benoit-Bird, K. J. and Lawson, G. L. (2016). Ecological insights from pelagic habitats acquired using active acoustics. *Annual Review of Marine Science*, 8:463–490. doi:10.1146/annurev-marine-122414-034001.
- Cornett, A., Toupin, M., and Nistor, I. (2015). Appraisal of the IEC technical specification for tidal energy resource assessment at minas passage, bay of fundy, canada. In *Proc. 2015 European Wave and Tidal Energy Conference (EWTEC), Nantes, France*.
- Dupont, F., Hannah, C. G., and Greenberg, D. (2005). Modelling the sea level of the upper bay of fundy. *Atmosphere-Ocean*, 43(1):33–47.
- Durand, N., Cornett, A., and Bourban, S. (2008). 3-d modelling and assessment of tidal current energy resources in the bay of fundy. *Canadian Hydraulic Centre, NRD, Ottawa, Report CHC-TR-052*.
- Fernandes, P., Gerlotto, F., Holliday, D., Nakken, O., and Simmonds, E. (2002). Acoustic applications in fisheries science: the ICES contribution. *ICES Marine Science Symposia*, 215:483–492.
- Guerra, M., Hay, A. E., Karsten, R., Trowse, G., and Cheel, R. A. (2021). Turbulent flow mapping in a high-flow tidal channel using mobile acoustic doppler current profilers. *Renewable Energy*, 177:759–772. doi:10.1016/j.renene.2021.05.133.
- Hasegawa, D., Sheng, J., Greenberg, D. A., and Thompson, K. R. (2011). Far-field effects of tidal energy extraction in the minas passage on tidal circulation in the bay of fundy and gulf of maine using a nested-grid coastal circulation model. *Ocean Dynamics*, 61:1845–1868. doi:10.1007/s10236-011-0481-9.
- Howard, A. G., Zhu, M., Chen, B., Kalenichenko, D., Wang, W., Weyand, T., Andreetto, M., and Adam, H. (2017). Mobilenets: Efficient convolutional neural networks for mobile vision applications. arXiv:1704.04861 [cs.CV].

- Hu, J., Shen, L., Albanie, S., Sun, G., and Wu, E. (2019). Squeeze-and-excitation networks. arXiv:1709.01507 [cs.CV].
- IPCC (2021). Summary for policymakers. *Climate Change 2021: The Physical Science Basis. Contributions of Working Group I to the Sixth Assessment Report of the Intergovernmental Panel on Climate Change.* Cambridge University Press.
- Jaccard, P. (1912). The distribution of the flora in the alpine zone.1. *New Phytologist*, 11(2):37–50. <https://nph.onlinelibrary.wiley.com/doi/pdf/10.1111/j.1469-8137.1912.tb05611.x>. doi:10.1111/j.1469-8137.1912.tb05611.x.
- Johannesson, K. and Mitson, R. (1983). Fisheries acoustics. a practical manual for aquatic biomass estimation. *FAO Fish. Tech. Pap.*, 240:249.
- Karsten, R., Greenberg, D., Tarbotton, M., Culina, J., Swan, A., O’Flaherty-Sproul, M., and Corkum, A. (2011). Assessment of the potential of tidal power from minas passage and minas basin (report no. 300-170-09-11. *Report by Acadia University.*
- Karsten, R. H., McMillan, J. M., Lickley, M. J., and Haynes, R. (2008). Assessment of tidal current energy in the minas passage, bay of fundy. *Proc. IMechE Part A: J. Power and Energy*, 222.
- Liu, L., Jiang, H., He, P., Chen, W., Liu, X., Gao, J., and Han, J. (2020). On the variance of the adaptive learning rate and beyond. In *Proceedings of the Eighth International Conference on Learning Representations (ICLR 2020)*.
- Lowe, S. C., Trappenberg, T., and Oore, S. (2021). LogAvgExp provides a principled and performant global pooling operator. arXiv:2111.01742 [cs.LG].
- Lowrie, W. E. (1968). Roosevelt and the passamaquoddy bay tidal project. *The Historian*, 31(1):64–89.
- O’Reilly, C., Solvason, R., and Solomon, C. (2005). Where are the world’s largest tides? In Ryan, J., editor, *BIO Annual Review*, pages 44–66. Fisheries and Oceans Canada and Natural Resources Canada: Bedford Institute of Oceanography, Dartmouth, Nova Scotia.
- Ronneberger, O., Fischer, P., and Brox, T. (2015). U-net: Convolutional networks for biomedical image segmentation. In Navab, N., Hornegger, J., Wells, W. M., and Frangi, A. F., editors, *Medical Image Computing and Computer-Assisted Intervention – MICCAI 2015*, pages 234–241, Cham. Springer International Publishing. ISBN 978-3-319-24574-4.
- Simmonds, J. and MacLennan, D. (2005). *Fisheries Acoustics Theory and Practice, 2nd edition.* Blackwell Publishing, Oxford, UK.
- Smith, L. N. (2015). No more pesky learning rate guessing games. *CoRR*, abs/1506.01186. arXiv:1506.01186.
- Smith, L. N. (2018). A disciplined approach to neural network hyper-parameters: Part 1 - learning rate, batch size, momentum, and weight decay. *CoRR*, abs/1803.09820. arXiv:1803.09820.
- Smith, L. N. and Topin, N. (2017). Super-convergence: Very fast training of residual networks using large learning rates. *CoRR*, abs/1708.07120. arXiv:1708.07120.
- Tan, M. and Le, Q. (2019). EfficientNet: Rethinking model scaling for convolutional neural networks. In Chaudhuri, K. and Salakhutdinov, R., editors, *Proceedings of the 36th International Conference on Machine Learning*, volume 97 of *Proceedings of Machine Learning Research*, pages 6105–6114. PMLR.
- Tong, Q., Liang, G., and Bi, J. (2019). Calibrating the adaptive learning rate to improve convergence of adam. arXiv:1908.00700 [cs.LG].
- Wright, L. (2019). Ranger - a synergistic optimizer. *GitHub repository.*
- Yong, H., Huang, J., Hua, X., and Zhang, L. (2020). Gradient centralization: A new optimization technique for deep neural networks. arXiv:2004.01461 [cs.CV].

Zhang, M. R., Lucas, J., Hinton, G., and Ba, J. (2019). Lookahead optimizer: k steps forward, 1 step back. arXiv:1907.08610 [cs.LG].